

Full length article

FIB-induced dislocations in Al submicron pillars: Annihilation by thermal annealing and effects on deformation behavior



Subin Lee ^a, Jiwon Jeong ^{a, b}, Youbin Kim ^c, Seung Min Han ^c, Daniel Kiener ^d, Sang Ho Oh ^{e, a, *}

^a Department of Materials Science and Engineering, Pohang University of Science and Technology (POSTECH), Pohang 37673, Republic of Korea

^b IBS Center for Integrated Nanostructure Physics (CINAP), Institute for Basic Science, Suwon 16419, Republic of Korea

^c Graduate School of Energy Environment Water and Sustainability, Korea Advanced Institute of Science & Technology (KAIST), Daejeon 34141, Republic of Korea

^d Department Materials Physics, Montanuniversität Leoben, Jahnstraße 12, 8700 Leoben, Austria

^e Department of Energy Science, Sungkyunkwan University, Suwon 16419, Republic of Korea

ARTICLE INFO

Article history:

Received 20 January 2016

Accepted 5 March 2016

Keywords:

Focused ion beam

Aluminum

Dislocations

Annealing

In-situ transmission electron microscopy

Slip bursts

ABSTRACT

In-situ transmission electron microscopy (TEM) annealing of submicron Al pillars (~300–450 nm in diameter) fabricated by focused ion beam (FIB) shows that the dislocation loops formed by the high energy Ga⁺ ion beam impact near the material surface can be removed by annealing at around half of the melting point (T_m). Quantitative analysis of real-time TEM data reveals that the dislocation loops first show a ripening behavior at around $0.4T_m$, i.e. larger loops coarsen at the expense of smaller ones. Subsequently, the ripened loops start to shrink and are eventually annihilated at $\sim 0.5T_m$ by the diffusion of thermally activated vacancies. Microcompression tests on the as-fabricated and annealed pillars suggest that the FIB-induced defects, particularly dislocation loops, distinctively affect the deformation behavior of submicron Al pillars; while the yield and flow stresses appear unaffected by the annealing, strain bursts are larger and more frequent in the annealed pillars compared to those of as-fabricated samples. In-situ TEM compression revealed that the initial plastic deformation and subsequent plastic flow of Al pillars are significantly altered by the presence of FIB-induced dislocation loops, as they actively respond to the applied stress. We observe that the initial dislocation activity in most FIB-prepared pillars was the glide of FIB-induced dislocation loops. With further straining, the dislocation loops escaped the pillar, leaving slip steps at the pillar surface and/or dislocation debris within the pillar volume via the interaction with other mobile dislocations. The subsequent dislocation slip is mostly localized at these locations, thereby forming large slip steps. Contrarily, in the case of annealed pillars, the deformation was rather homogeneous with the formation of multiple fine slip steps. The present direct TEM observations contribute to the understanding of the nature of FIB-induced defects and reveal their distinct roles in the deformation behaviors of submicron pillars.

© 2016 Acta Materialia Inc. Published by Elsevier Ltd. All rights reserved.

1. Introduction

Size effects in mechanical properties of face-centered cubic (fcc) single crystals have attracted tremendous interest since Uchic et al. reported that the yield strength of single crystal Ni pillars increases as the pillar diameter decreases to micron or submicron sizes [1–4]. This phenomenon is referred to as “smaller is stronger”, and is now understood as a common feature of single crystal metallic

materials, valid not only for fcc but also for body-centered cubic [5–7] and hexagonal close-packed metals [8,9]. Several models have been suggested to explain the mechanical size effects. One is the source truncation model, which is based on an increase of the average stress for the activation of dislocation sources with decreasing sample size [10,11]. The other model is based on the exhaustion of mobile dislocations due to the limited glide distance from a source to the pillar surface and thus the lack of mutual interaction with other dislocations, which limits possible multiplication processes [12,13].

Most of the experimental work on mechanical size effects has been conducted through microcompression testing of single crystal

* Corresponding author. Department of Energy Science, Sungkyunkwan University, Suwon 16419, Republic of Korea.

E-mail address: sanghooh@skku.edu (S.H. Oh).

pillars fabricated by using a focused ion beam (FIB). The high energy Ga⁺ ion beam used for FIB milling, however, is known to induce various structural defects near the pillar surface, such as vacancies, interstitials, and also their aggregates forming stacking fault tetrahedra or dislocation loops [14]. The damaged region containing such defects extends up to several tens of nanometers from the surface, of which the exact thickness varies depending on the milling condition and target material [15,16]. These FIB-induced defects, particularly dislocation loops, may critically affect the deformation behavior and/or the mechanical properties of FIB-prepared pillars. For instance, the effects of FIB milling were investigated by dislocation dynamics simulations, showing that the flow stress of submicron fcc pillars with a diameter in the range of 0.5–1.0 μm increases by 10–20% due to dislocation pile up at the damage layer [17]. A FIB-induced surface hardening effect was also observed experimentally for single crystal Mo alloys when increasing the acceleration voltage of the Ga⁺ ion beam during FIB milling [18,19]. Kiener et al. reported that the flow stress of FIB-fabricated Cu pillars can increase due to the solid solution hardening effect of Ga in Cu [20]. All these studies suggest that FIB milling alters not only the strength, but also the plastic flow characteristics of metals in small dimensions.

Removal of FIB-induced defects is therefore crucial for exploring the true mechanical size effects and inherent deformation behavior of metal pillars. Shan et al. showed that FIB-induced dislocation loops in Ni pillars can be removed by applying a small amount of (plastic) strain, which was coined as “mechanical annealing” [21]. Another practically more acceptable way to remove FIB-induced defects would be a thermal annealing. Unwanted formation of a surface oxide or contamination layer can be suppressed by conducting the annealing in high vacuum. Recently, Lowry et al. reported that the yield stresses of FIB-prepared Mo pillars are recovered close to the theoretical strength after thermal annealing [22]. Similar results were also obtained by Kiener et al. for Cu pillars [23]. Although several previous studies have shown that the FIB-induced defects affect the mechanical properties of metal pillars and this can also be modified by thermal annealing, the basic thermal processes leading to defect annihilation, as well as the detailed role of these defects in the stochastic plastic deformation of small volumes, are still not understood well.

In the present study, to elucidate the underlying mechanisms controlling the annihilation of FIB-induced dislocation loops and their influences on the mechanical properties and the deformation behavior of metal pillars, we carried out in-situ transmission electron microscopy (TEM) annealing, as well as in-situ TEM compression experiments of as-prepared and annealed Al submicron pillars. We chose Al as a model fcc metal because a moderate annealing below 200 °C is quite effective to remove most of the FIB-induced defects due to its low melting point (T_m). When a FIB-prepared Al pillar is annealed in TEM, the dislocation loops first exhibit ripening behavior at $0.4T_m$, followed by their annihilation, which is facilitated by the diffusion of thermally activated vacancies as the temperature approaches $0.5T_m$. The in-situ TEM compression directly shows that in the FIB-prepared pillars the first dislocation activity was the expansion and glide of the FIB-induced dislocation loops, resulting in the formation of slip steps on the surface and/or immobilized dislocations through interactions with other dislocations. Upon further deformation dislocation slip localized at these locations, thus forming large slip steps. Contrarily, in the case of annealed pillars, slip steps are distributed more uniformly along the pillar axis. One of the most pronounced differences in the deformation behavior of the two types of pillars is the strain burst distribution; the average strain and the load drop per strain burst event were much larger in the annealed pillar compared to those in the as-prepared one. This clearly demonstrates that the FIB-

induced defect influence the nanoscale deformation of Al pillars by affecting dislocation escape processes.

2. Experimental procedures

2.1. Fabrication of Al pillars using FIB

A (111)-orientated Al single crystal was polished and subsequently etched with a diluted hydrofluoric acid etchant to remove the native surface oxide. Submicron pillars were fabricated onto this polished surface using a FIB (Quanta 3D FEG, FEI, Hillsboro, OR). First, a thin lamella was lifted out from the Al single crystal and then attached onto a supporting Cu grid by using Pt deposition. Then, coarse micropillars with a radius of 10 μm were fabricated using the Ga⁺ ion beam with a beam current of 15 nA at 30 kV in an annular milling mode. During the consecutive fine FIB milling of the pillars, the ion beam current was gradually decreased to reduce ion beam damage, and 10 pA were used for the final polishing step. The prepared pillars had a diameter in the range of ~300–450 nm at mid sample height and a length of around 1 μm, giving them an aspect ratio of ~3:1, well suited for microcompression experiments [24]. The aspect ratio of the pillars prepared for in-situ TEM compression, however, was higher than 3:1, specifically around 5:1 in average. This aspect ratio was chosen to secure a sufficient field-of-view of the pillar when viewed from the side in TEM while minimizing the bending or buckling [25]. A scanning electron microscopy (SEM) image of a representative FIB-prepared pillar is shown in Fig. 1a. A slight taper of ~3° is unavoidable using this top down annular milling approach [26,27]. The insert in Fig. 1a depicts the orientation of the Thompson tetrahedron. Since the loading direction is aligned closely parallel to the [111] direction, there are six slip systems with a Schmid factor of ~0.27 on the three inclined slip planes, (a), (b) and (c) according to the Thompson tetrahedron notation.

In order to estimate the thickness of the FIB-induced surface damage layer, the trajectory of Ga⁺ ions was simulated using the SRIM software package [28], see Fig. 1b. The parameters employed for the final stage of FIB milling were used for the simulation, which are: an acceleration voltage of 30 kV, a beam current of 10 pA, and an incidence angle of 89.0° [27]. Note that the SRIM code does not take into account any channeling effect of the incoming Ga⁺ ions which might arise for a highly symmetric low-index crystal orientation as in the present case.

2.2. Transmission electron microscopy: in-situ annealing, in-situ compression, and X-ray elemental mapping

A TEM (JEM-2100F, JEOL Ltd., Tokyo, Japan) operated at 200 kV was used for in-situ TEM experiments. Using a double tilt heating holder (Gatan 654, Gatan Inc., Pleasanton, CA) the heating experiments were carried out following two different routes. In the first annealing treatment, the FIB-prepared pillars were heated to 120 °C within 10 min, and then the temperature was increased to 200 °C in 10 °C steps after stabilization for 10 min at each temperature. This was intended for the clear observation of microstructural changes with minimizing a sample drift. In the second heating route, an isochronal annealing was conducted at a constant ramping rate of 5 °C/min for a quantitative assessment of the activation energy of the dislocation annihilation process. To document the temporal evolution of FIB-induced dislocation loops, real-time TEM movies were recorded using a charge coupled device camera (ORIU5 200D, Gatan Inc., Pleasanton, CA) at 25 frames per second. The size of the dislocation loops was determined by manual measurement of the projected area of the loops on the snapshot TEM images with minimizing the errors by applying a Canny edge detection filter to the selected regions of uniform contrast.

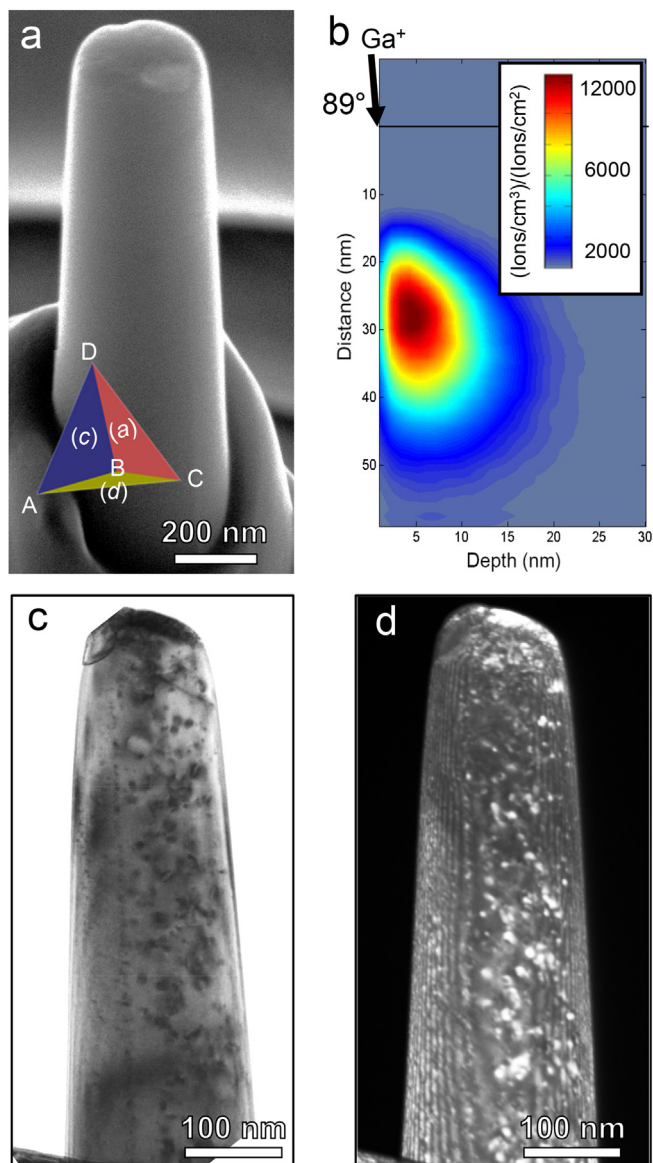


Fig. 1. (a) SEM image of a submicron Al pillar fabricated by FIB milling. A Thompson tetrahedron is inserted to indicate the orientation of {111} slip planes with respect to the loading direction, which was determined precisely by electron diffraction in the TEM. (b) Ion trajectory simulation by SRIM. The penetration depth of Ga⁺ ions is calculated to be ~20 nm, with a peak concentration at ~5 nm beneath the surface. (c–d) TEM bright-field and dark-field images of a FIB-fabricated pillar showing the presence of small dislocation loops near the surface.

In-situ TEM compression tests were carried out to obtain a detailed insight into the deformation behavior of as-FIB-prepared and annealed Al pillars. A nanoindentation TEM holder (TEM-indenter, Nanofactory Instrument, Goteburg, Sweden) equipped with a flat diamond punch tip was used. The compression tests were carried out at a displacement rate of 0.5 nm s⁻¹, which ensured recording of a large number of video frames (25 frames per second) for subsequent in-depth analysis.

In order to characterize the spatial distribution of Ga atoms after the annealing of pillars, X-ray energy dispersive spectroscopy (EDS) was carried out using a Cs-corrected scanning transmission electron microscope (STEM) (JEM-ARM200F, JEOL Ltd., Tokyo, Japan).

2.3. Ex-situ microcompression tests

Ex-situ microcompression tests were conducted for quantitative assessment of the mechanical properties and deformation characteristics of the as-FIB-prepared and annealed Al pillars. The annealing was performed at 180 °C for 30 min in a high vacuum furnace (~10⁻⁶ Pa). This condition was chosen based on the in-situ TEM heating experiments and found to be effective for removal of most of the FIB-induced dislocations in Al pillars. For both, FIB-prepared and annealed pillars, five samples with slightly different diameters were tested; the diameters of the FIB-prepared pillars are in the range of 347–430 nm, while for the annealed pillars they range from 325 to 430 nm. Uniaxial compression of the Al nanopillars was performed by using a nanoindentation system (TI 750 Ubi, Hysitron Inc, Minneapolis, MN) with a flat-ended diamond punch at a displacement rate of 2.4 nm s⁻¹, corresponding to an engineering strain rate of 0.002 s⁻¹. The stress versus strain plots were calculated using a constant-volume, homogeneous deformation model taking into account the sample sink-in [29–31]. The yield stress was determined at the 0.2% offset strain, and the flow stress was defined as the stress at 5% strain in the stress–strain curve.

3. Results and discussion

3.1. FIB-induced dislocations

TEM observation of the as-fabricated Al pillars revealed the formation of a few nm-sized dislocation loops, as shown in Fig. 1c and d. According to the ion trajectory simulation, the penetration depth of the Ga⁺ ion beam is calculated to be ~20 nm, with a peak concentration at ~5 nm beneath the surface (Fig. 1b). Some of the Al atoms within this region are likely to be displaced from their atomic sites upon impingement of the Ga⁺ ions, and as a result, point defects such as vacancies and self-interstitials are generated. Aggregation of the point defects can result in the formation of dislocation loops. According to Idrissi et al., the dislocation loops formed by a high energy Ga⁺ ion impact in Al at room temperature are most likely of an interstitial type [32]. Such FIB-induced dislocation loops are clearly visible in bright-field (Fig. 1c) and dark-field (Fig. 1d) TEM images, as the strain fields associated with the dislocation loops produce pronounced diffraction contrast. Quantitative analysis of TEM images yields that the average diameter and the density of the dislocation loops in the present case are 2.5 ± 0.4 nm and 3.4 × 10¹⁴ m⁻², respectively, in good accordance with literature reports [33].

3.2. Annihilation of FIB-induced dislocations by annealing

Annealing of the as-prepared Al pillars inside the TEM directly visualizes the thermal processes leading to the annihilation of FIB-induced dislocation loops. The TEM images shown in Fig. 2a–e capture the evolution of FIB-induced dislocation loops with temperature (also refer to Supplementary Video S1). Fig. 2f shows the quantitative measurements of the number, average radius, and total area of the dislocation loops at each temperature. The dislocation loops show no significant change in size and number up to 130 °C (Fig. 2b and f). As the temperature is increased above 140 °C, which corresponds to a homologous temperature ($T_H = T/T_m$) of 0.44 for Al, the dislocation loops show a ripening behavior, i.e. smaller loops shrink whereas larger loops expand, resulting in an increase of the average size but a decrease in the number of loops (Fig. 2f). The ripening behavior continues up to 170 °C ($T_H = 0.47$) (Fig. 2c). When the temperature is increased further and approaches a T_H of 0.5, the total loop area, which remained almost unchanged during the ripening stage, starts decreasing, eventually

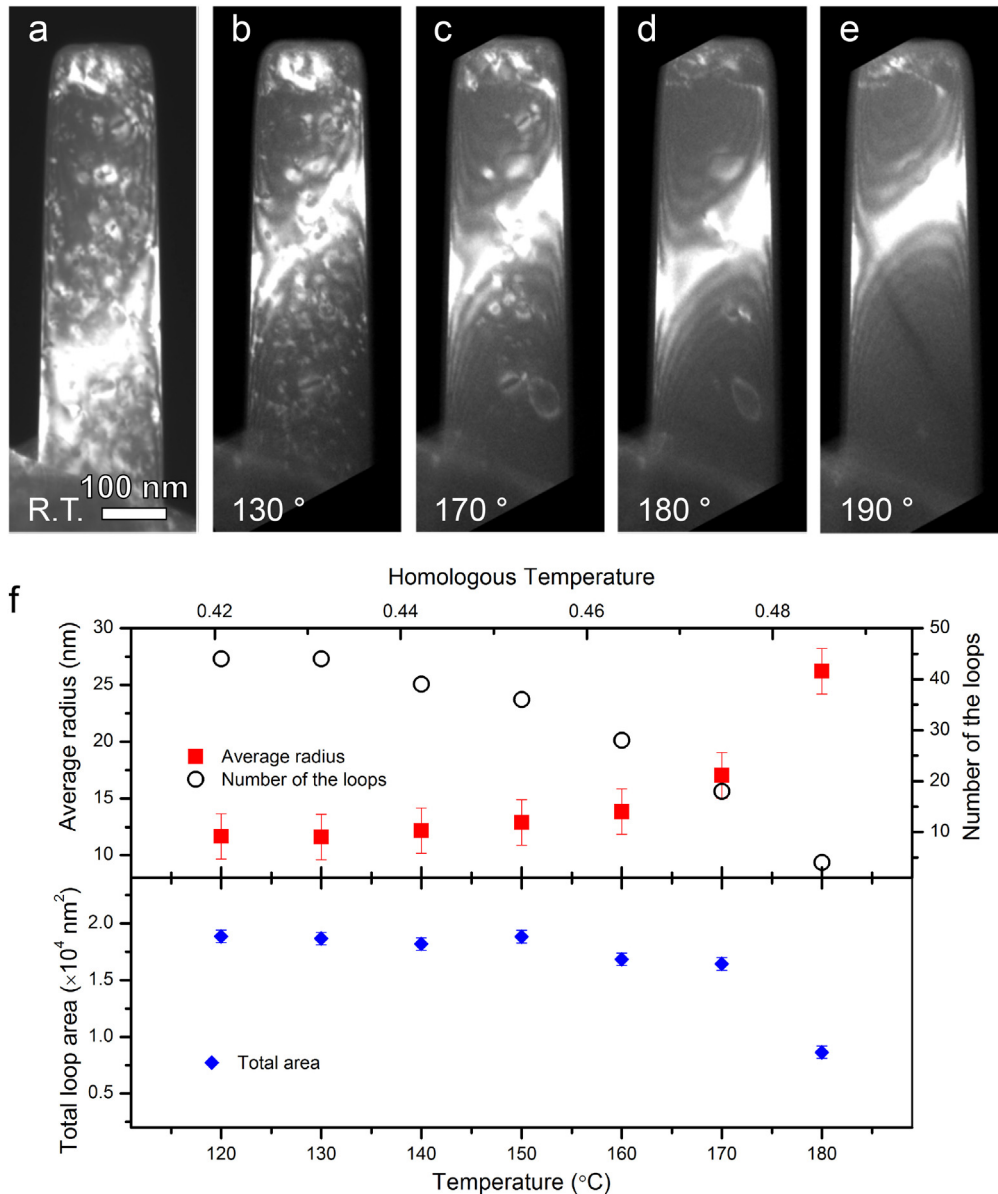


Fig. 2. Sequence of TEM images captured during the thermal annealing of a FIB-prepared Al pillar at (a) room temperature; (b) 130 °C; (c) 170 °C; (d) 180 °C; (e) 190 °C. After an initial ripening behavior below 170 °C, dislocation loops were annihilated above this temperature, leaving an almost dislocation-free pillar at 190 °C. The real-time TEM movie is provided as Supplementary Video S1. (f) Evolution of the average radius (red square), number (open circle) and area (blue diamond) of dislocation loops with annealing temperature.

resulting in the annihilation of almost all dislocation loops (Fig. 2d–e). The annihilation of dislocation loops occurred via either escape through the pillar surface or continuous internal shrinkage. The latter process was slower than the former and thus is regarded as the rate-limiting step of the dislocation annihilation process in the present case (refer to Fig. 3d).

Supplementary video related to this article can be found at <http://dx.doi.org/10.1016/j.actamat.2016.03.017>.

In order to verify the thermal processes leading to the annihilation of dislocation loops, an isochronal heat treatment was conducted by increasing the temperature from room temperature to 200 °C at a constant ramping rate of 5 °C/min (Fig. 3 and Supplementary Video S2). The TEM images shown in Fig. 3a highlight the evolution of the FIB-induced dislocation structure with temperature. The radius of individual loops was measured at every 10 °C increment from 150 °C to 180 °C and Arrhenius plots were

constructed by plotting the dislocation loop area as a function of $1/T$ (Fig. 3b). Note that the dislocation loop areas are plotted on log scales and normalized by those measured at 130 °C, the lowest temperature at which individual dislocation loops can be clearly resolved. Since the dislocation loops appeared to annihilate via different routes in TEM movies, i.e. internal shrinkage or surface escape, we executed several different Arrhenius analyses using various data sets of loop area, for example, the total loop area or individual loop areas (indicated by Loop 2 and Loop 3 in Fig. 3a).

Supplementary video related to this article can be found at <http://dx.doi.org/10.1016/j.actamat.2016.03.017>.

The activation energy (E_a) determined from the Arrhenius analysis of the total loop area is 0.32 ± 0.02 eV, while that from the individual loop is 1.35 ± 0.06 eV for Loop 2 and 1.47 ± 0.01 eV for Loop 3 (Fig. 3b), respectively. The measured E_a for the internal shrinkage of individual loops is comparable to the sum of vacancy

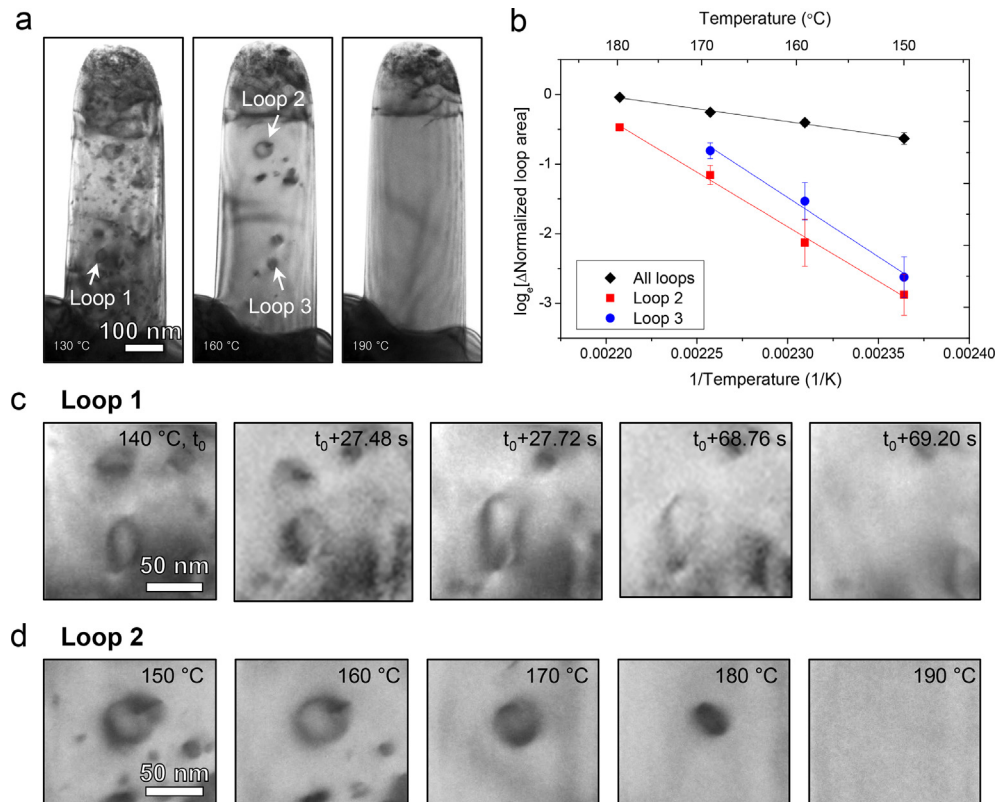


Fig. 3. Analysis of the annihilation process of dislocation loops during isochronal annealing of FIB-prepared Al pillar in the TEM for a temperature ramping rate of 5 °C/min. (a) TEM images taken at temperatures of: 130 °C (left); 160 °C (middle); 190 °C (right) while increasing the temperature to 200 °C. (b) Arrhenius plot of normalized dislocation loop areas as a function of $1/T$. Two activation energies were calculated, where one tracks the change in the area within all loops, which amounts to ~ 0.32 eV, while the measure from single dislocation loops, indicated as Loop 2 and Loop 3, is ~ 1.35 eV and ~ 1.47 eV, respectively. (c) TEM snapshots showing the temporal evolution of Loop 1 at 140 °C, which escaped through the surface. (d) TEM snapshots showing the evolution of Loop 2 with temperature, which shrank by vacancy diffusion.

formation and migration energies in Al, which are reported as 0.66 eV and 0.62 eV, respectively [34,35]. It is proposed that the equilibrium vacancy concentration increases rapidly as the temperature increases to $T_H \sim 0.5$, and the proliferated vacancies diffuse towards the interstitial dislocation loops, thereby facilitating the internal shrinkage and complete annihilation of dislocation loops. It is likely that the vacancies are preferentially formed from the surface, because the formation energy is about 0.2 eV lower at the surface than in the bulk [36]. On the other hand, the lower E_a determined from all cumulative loops indicates that dislocation loops were annihilated not only by vacancy diffusion, but also by other processes with lower energy barriers, for example, glide and escape through the free surface. As illustrated by an example shown in Fig. 3c, some dislocation loops (Loop 1) expanding near the surface get attracted to the surface, probably under the influence of the surface image force, and escape the crystal very quickly within a second. Notably, this occurs at much lower temperatures (e.g. 140 °C in Fig. 3c) than the internal shrinkage (e.g. 190 °C in Fig. 3d).

3.3. Effects of FIB-induced dislocations on mechanical properties

The stress–strain curves obtained by microcompression of five pillars for each type are shown in Fig. 4a and c. At first glance, the two differently prepared sets of pillars exhibit similar stress–strain curves which consist of multiple discrete slip bursts with a similar level of yield and flow stresses. The yield stresses of the FIB-prepared and annealed pillars are measured to be 368 ± 59 MPa and 370 ± 72 MPa, respectively, as summarized in Fig. 4e. This

indicates that for this particular size range of Al [111] pillars, the stress required for dislocation nucleation is not greatly altered by the annealing treatment. One may find a clue to this from the fact that dislocations are not completely removed, but remained after annealing (refer to Fig. 11). All annealed pillars revealed the presence of residual dislocations near the top of the sample, a region of high Ga concentration (will be discussed in section 3.7) and also a region of initial plastic deformation (will be discussed in section 3.5). As the yield event is thus governed by pre-existing dislocations in both pillars, yielding occurs at a similar stress level since the size of potential dislocation sources is similar in both pillars.

Taking a close look at the stress–strain curves, one can find that the strain burst characteristics are different for the two types of pillars. Therefore, we focus more on the analysis of the strain burst distributions rather than the stress values. First of all, at small strain values it is seen that the as-FIBed pillars exhibit an individual large load drop, while the annealed pillars show multiple smaller load drops (Fig. 4b and d), indicating that dislocation slip is more likely to be localized in the presence of pre-existing dislocations in the as-FIBed pillars.

However, according to the results summarized in Fig. 4e for large strain values, the annealed pillars show a larger magnitude of strain bursts than the FIB-prepared ones. The fraction of strain bursts contributing to the total deformation was also higher in the annealed pillars. Moreover, in the annealed pillars complete load drop to zero stress occurred more frequently, and thus the averaged amount of load drops was also larger compared to the FIB-prepared pillars. Though the error bars, which represent the standard deviation of statistics, are relatively large, it is as

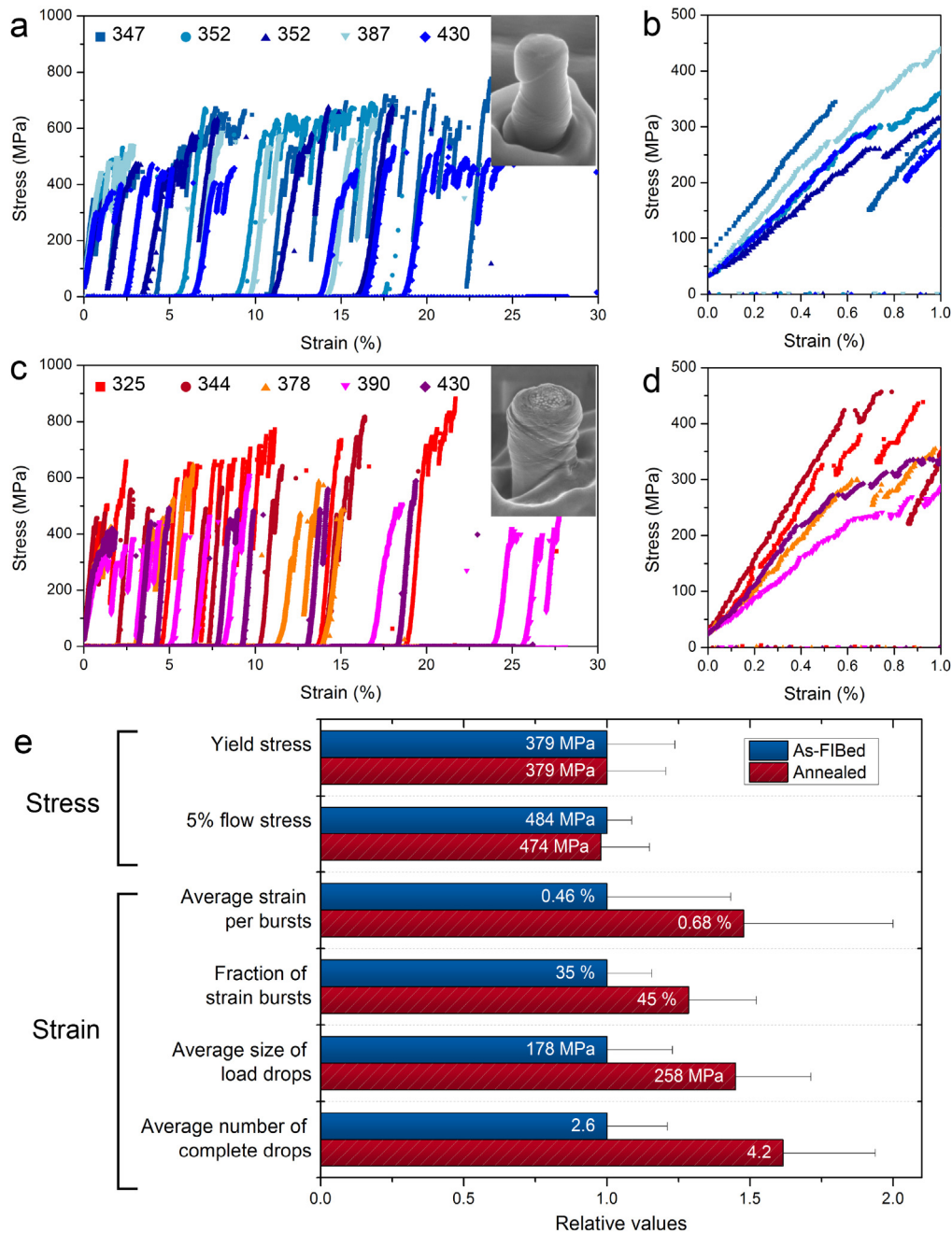


Fig. 4. Stress–strain curves obtained by microcompression tests of (a) FIB-prepared and (c) annealed pillars. For both, FIB-prepared and annealed pillars, five samples with slightly different diameters were tested. SEM images of deformed pillars were included as insets for comparison. (b, d) Zoom-in of the small strain regime (up to 1%) of stress–strain curves for FIB-prepared (b) and annealed (d) pillars. (e) Analysis of the slip characteristics of FIB-prepared and annealed pillars. While the yield and flow stresses are similar, the load drops and strain burst characteristics are distinctly different between the two types of pillars. All values were normalized by that of the FIB-prepared samples for ease of comparison. The error bars represent the standard deviation. The larger strain burst (and larger load drop) with larger standard deviations of the annealed pillars indicate more stochastic deformation responses.

expected given the typical stochastic deformation behavior of nanopillars rather than inaccuracies in the measurement. Based on this statistical data, we could hypothesize that there should be more sources or nucleation points in annealed pillars, and mobile dislocations should travel larger distances compared to the FIB-prepared pillars. To test this hypothesis and elucidate the origin of these differences in slip statistics in correlation with defect structures of the pillars, in-situ TEM deformation tests were conducted as below.

3.4. Role of FIB-induced dislocations in the plastic deformation – Yield and dislocation source formation

In-situ TEM compression shows that the plastic deformation of FIB-prepared pillars initiates by the consecutive processes of expansion, glide and escape of FIB-induced dislocation loops (Supplementary Video S3), demonstrating that they actively respond to the applied stress and therefore play a critical role in determining the yield stress. The TEM snapshot images shown in Fig. 5 capture the first dislocation activity taking place during

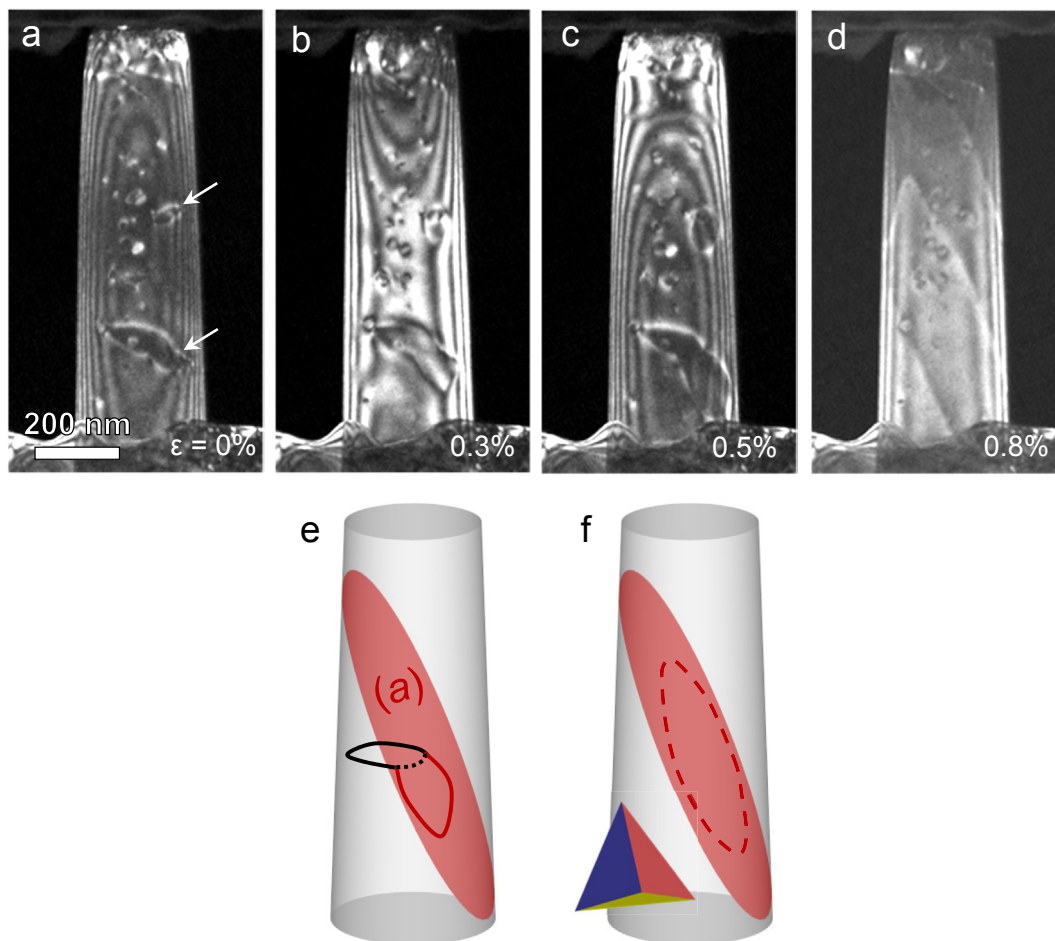


Fig. 5. In-situ TEM observation of the initial plastic deformation of a FIB-prepared Al pillar (refer to Supplementary Video S3). (a) TEM dark-field image of the FIB-prepared pillar before deformation. The two largest dislocation loops are indicated by arrows. Note that the dislocation density of the Al pillars prepared for in-situ TEM (as well as those shown in 6a and 7a) is around an order of magnitude lower than that of the as-FIB-prepared pillars due to a slight annealing effect caused by the fixation process. (b) Initial response of the dislocation loops at a strain of $\sim 0.3\%$. (c) Glide of the glissile segment on an (a) plane. (d) Escape of the dislocation loops through the surface and concurrent formation of slip steps. (e, f) Schematic diagrams showing the escape process of the dislocation loop.

compression of a FIB-prepared pillar. At a strain of $\sim 0.3\%$, the dislocation loops, particularly the largest ones (e.g. those indicated by white arrows in Fig. 5a), expand and lay down a segment on the $(1\bar{1}1)$ slip plane, i.e. the (a) plane in the Thompson notation (Fig. 5b and e). Subsequently, the glissile segment of the loop glides toward the surface of the pillar, where it escapes and forms a slip step (Fig. 5d and f).

Supplementary video related to this article can be found at <http://dx.doi.org/10.1016/j.actamat.2016.03.017>.

The FIB-induced dislocation loops not only control the yielding of the Al pillar, but also play an important role in the formation of dislocation sources. Fig. 6 and Supplementary Video S4 present an example of the formation of a dislocation source from a FIB-induced dislocation loop. Similar to Fig. 5, a FIB-induced dislocation loop (yellow arrow in Fig. 6a) expands under the applied stress (Fig. 6b). Consecutively, the expanding loop interacts with another dislocation in motion on plane (b) (indicated as red line in Fig. 6c). Such a dislocation interaction in the small confined volume of pillar usually results in the line opening of dislocation loop and also leaves the remaining dislocation on another slip plane, e.g. the (c) plane as shown in Fig. 6d. While one end of this dislocation, indicated by the white arrow in Fig. 6e, is pinned within the sample, the other one is connected to the free surface, thereby acting as a single-armed dislocation source. This source emits new

dislocations and increases the dislocation density to $\sim 10^{14} \text{ m}^{-2}$ (Fig. 6f).

Supplementary video related to this article can be found at <http://dx.doi.org/10.1016/j.actamat.2016.03.017>.

To validate the role of FIB-induced dislocation loops on the strength quantitatively, the shear stress required to activate the dislocation source was calculated. As mentioned above, the dislocation loop indicated by the arrow in Fig. 6a expands and subsequently transforms to a dislocation source. The critical shear stress required for the activation of the loop as a source is determined using the equation, $\tau_0 = \alpha Gb/R$ [37,38]. Hereby, G is the shear modulus of Al (26 GPa), and b is the magnitude of the Burgers vector (0.286 nm). R is the radius of the loop, which was measured to be 50 nm in the TEM image, and the constant α is in the range ~ 0.5 – 1.0 , where 0.7 was used here, resulting in a critical shear stress of ~ 104 MPa. Ignoring a slight deviation of the loading axis from the $[111]$ crystal orientation, there are six $[011](1\bar{1}1)$ slip systems with a Schmid factor of 0.27. Thus, the normal stress required to activate the dislocation is ~ 386 MPa. This value is in good agreement with the measured yield stress of FIB-prepared pillars (368 ± 59 MPa), and also consistent with the extrapolation of data from previous reports on larger samples [39], confirming that dislocation loops formed by the FIB process play a decisive role in governing the yield stress and subsequent plastic deformation.

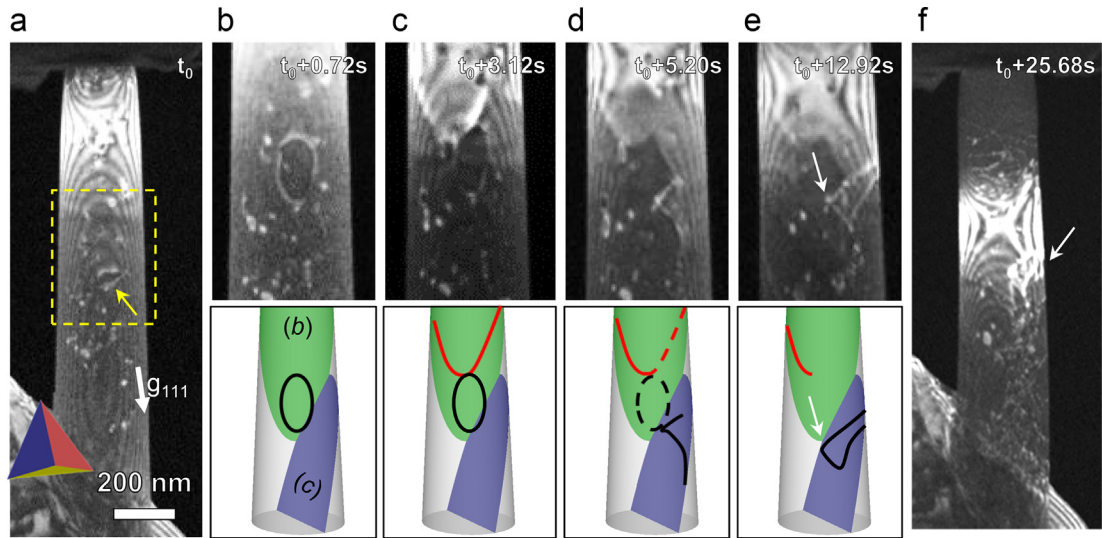


Fig. 6. In-situ TEM observation showing the formation of a dislocation source from FIB-induced dislocation loops (refer to Supplementary Video S4). (a) TEM dark-field image showing the FIB-prepared pillar before deformation. Enlarged images of the dashed box in (a) during compression and corresponding schematics are shown side by side in (b)–(e): (b) Expansion of the dislocation loop indicated by a yellow arrow in (a) under stress. (c) Interaction of the loop with another dislocation gliding from the top part of pillar on a (b) slip plane. (d) Intersection of the expanding loop with the surface, which leaves dislocation debris behind. (e) Formation of a slip step on the surface, while the moving arm is arrested at the surface. (f) Avalanche-like dislocation emission from the source developed near the slip step indicated by a white arrow. (For interpretation of the references to colour in this figure legend, the reader is referred to the web version of this article.)

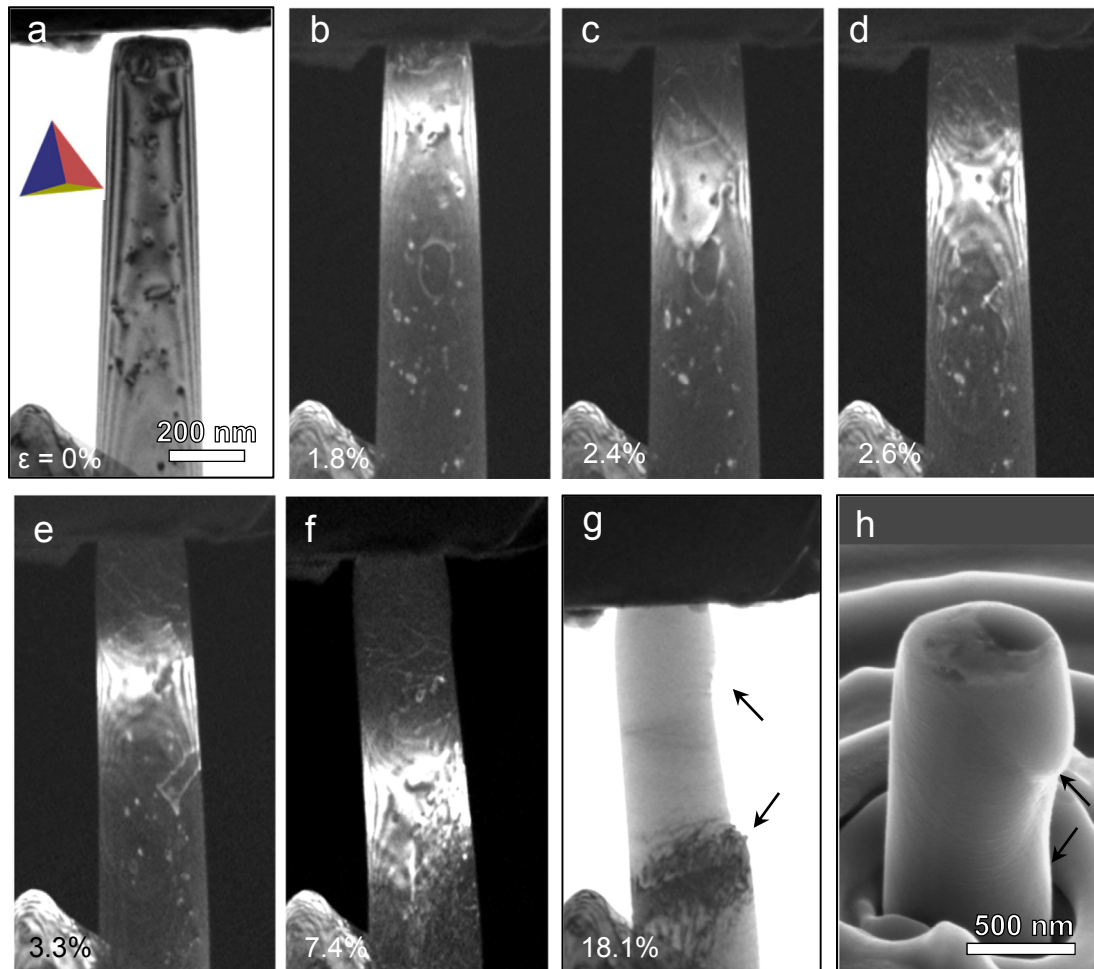


Fig. 7. In-situ TEM observation of the whole deformation process of a FIB-prepared pillar. (a) TEM bright-field image of the pillar before deformation. (b) Initial deformation by the expansion of FIB-induced dislocation loops. (c) Interaction between the dislocation loop and mobile dislocations. (d) Escape of the dislocation loop through the surface, and (e) formation of a dislocation source near the surface. (f) Localized dislocation slip by avalanche-like dislocation emission from the source. (g) Slip localization at the two dominating large slip steps (black arrows). (h) SEM image of a deformed pillar showing two large slip steps (black arrows). Note that the SEM image was recorded from another deformed pillar after the ex-situ microcompression test.

3.5. Effects of FIB-induced dislocations on the plastic deformation after yield – Slip localization

As we already mentioned, the FIB-induced dislocation loops critically affect the initial deformation. However, it does not mean that all of the dislocation loops act as sources since most of them quickly escape through the surface (i.e. mechanical annealing). Actually, only a few dislocations loops become dislocation sources after interactions with other dislocations. Once dislocation sources form, they dominate the subsequent deformation and result in localized slip, as is the case for as-FIBed pillars. Fig. 7 and Supplementary Video S5 summarize the overall deformation process of an as-prepared pillar. In the plastic flow regime after yielding, the deformation is carried mainly by the dislocations emitted from the sources developed preferentially near the boundaries of the pillar, i.e. near the contact with the punch (top end; Fig. 7c) or near the base of the pillar (bottom corner; refer to Fig. 8), from which dislocations are emitted into the central region of the pillar. This preference might arise from stress localization due to the tapering effect, local asperity contacts with the punch, and/or the boundary conditions of the pillar whose bottom mount is free to move in the current deformation setup [40]. The emitted dislocations usually undergo an interaction with pre-existing dislocation loops before they escape through the surface (Fig. 7d and e), leaving slip steps and dislocation debris behind. Subsequent deformation is typically localized at one of these slip steps because of local stress concentrations assisting the dislocation nucleation process (Fig. 7f and g). As shown by the SEM image of the deformed pillar (Fig. 7h), the tested samples usually exhibit one or two large slip steps, which agree well with the TEM observations.

Supplementary video related to this article can be found at <http://dx.doi.org/10.1016/j.actamat.2016.03.017>.

Although a local fluctuation of dislocation density is quite common during the deformation of submicron pillars due to the localized and discrete nature of dislocation slip events [41,42], the dislocation density averaged over the entire sample remains quite high, since not all of the nucleated dislocations can escape. Fig. 8 and Supplementary Video S6 present an example showing how local deformation is produced by a remote dislocation source developed at the base of an as-FIBed pillar. While one end of the emitted dislocations is still connected to the pinning point of the single-armed source, the other end immediately approaches the surface upon emission (yellow arrows in Fig. 8a and c). The dislocations undergo cross-slip from (c) plane to (a) plane to reach a location of high shear stress, where they escape through the surface and leave a slip step behind (white arrows in Fig. 8b and d), as schematically illustrated in Fig. 8f. As the source operation continues over several cycles, the slip step extends further, causing strain localization as shown in Fig. 8e. The behavior of this dislocation source is quite similar to that of a spiral source observed experimentally in an Al fiber [38], as well as several computational studies [41,42].

Supplementary video related to this article can be found at <http://dx.doi.org/10.1016/j.actamat.2016.03.017>.

3.6. Deformation behavior of annealed pillars

For comparison, an annealed Al pillar was deformed in-situ in the TEM (Fig. 9 and Supplementary Video S7). This sample was almost free of dislocations except for a few that remained near the contact area after annealing (Fig. 9a and also refer Fig. 11), which play a critical role in determining the yield strength by formation of a dislocation source nearby similar to the FIB prepared pillars (Fig. 9b). The TEM observation hints that the stress required for dislocation nucleation is not greatly different from that for the FIB-

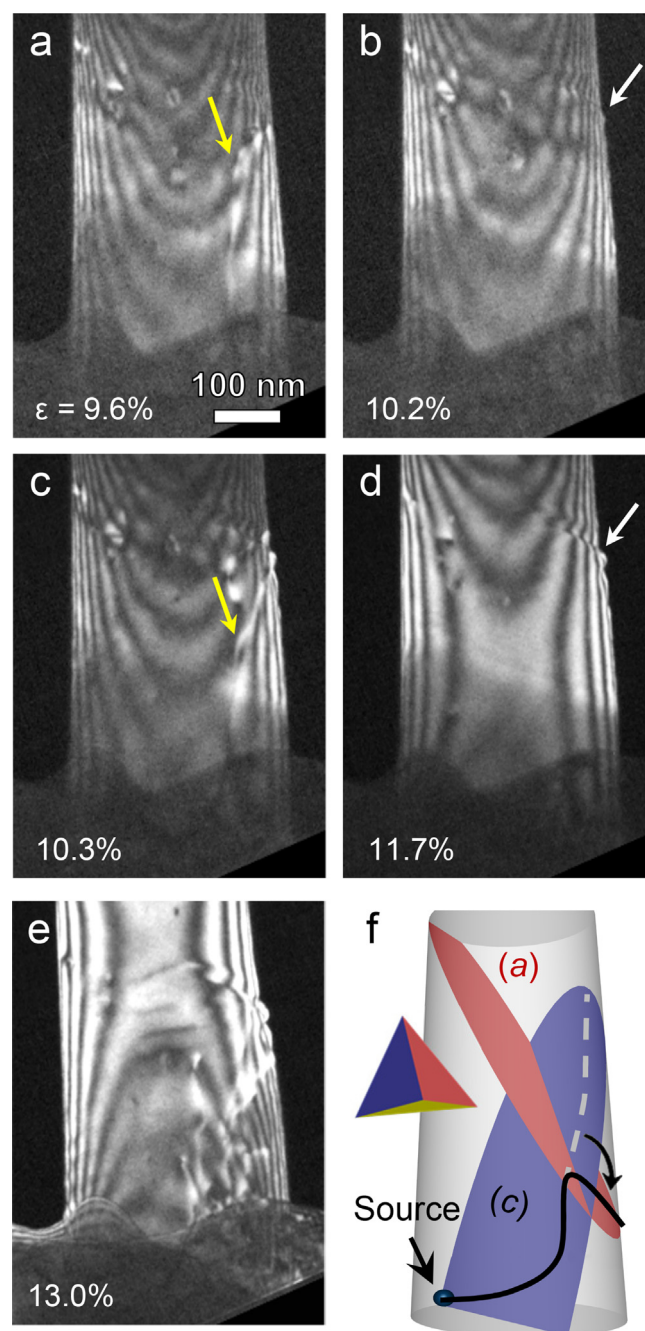


Fig. 8. Localized dislocation slip by operation of a single-armed spiral source in an as-FIB prepared Al pillar. (a, b) A single-armed dislocation source operation at the bottom region of the pillar via dislocation nucleation (yellow arrow) and escape leaving surface steps (white arrow). (c, d) The dislocations undergo cross-slip from (c) plane to (a) plane to reach the location of high shear stress (white arrow), where they escape through the surface with forming slip steps. (e) Increased dislocation density near the dislocation source by successive source operation causing deformation to become highly localized. (f) Schematic model of the dislocation process. (For interpretation of the references to colour in this figure legend, the reader is referred to the web version of this article.)

prepared pillars, due to similar dislocation structures at the top part of the pillars. Deformation is continued at the bottom part of the pillar by dislocation nucleation after a slight bending of the sample (Fig. 9c). Upon further loading, the strain is accommodated mostly by dislocations nucleated from the side surface and their unhindered escape processes at the opposing surface (Fig. 9d and e), in strong contrast to the FIB-prepared pillars. Importantly, the

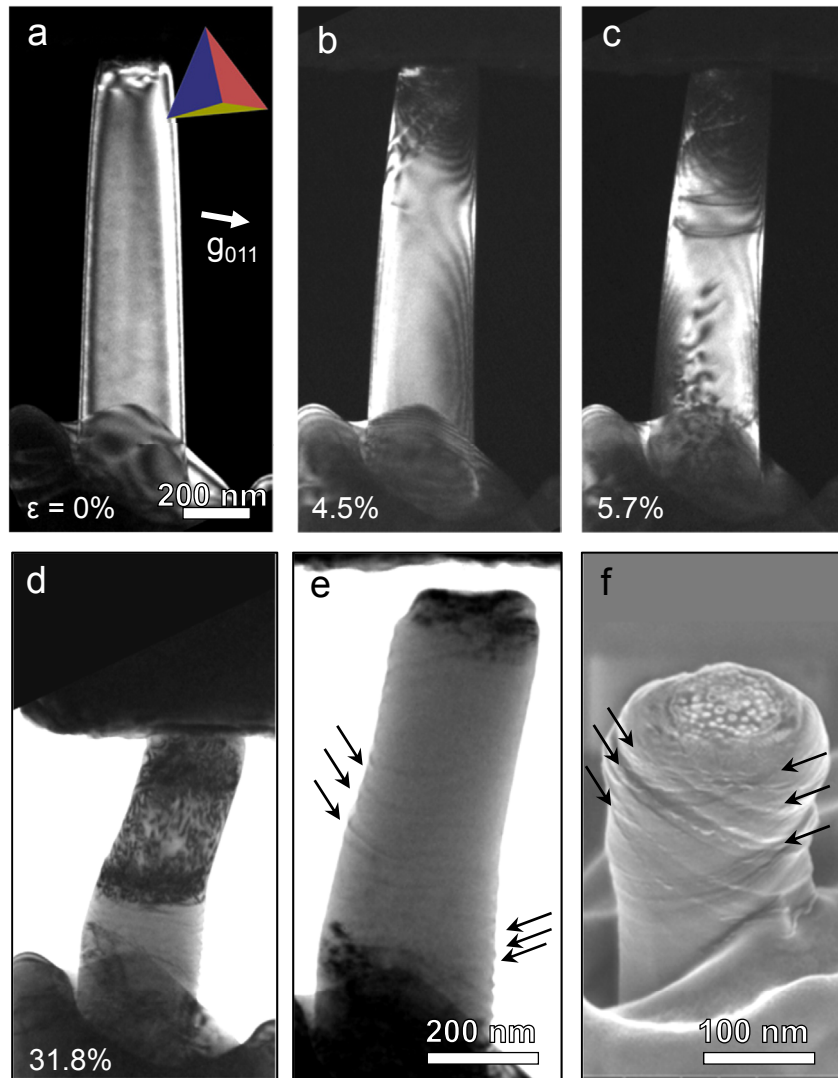


Fig. 9. In-situ TEM observation of the complete plastic deformation process of an annealed pillar (refer to Supplementary Video S7). (a) TEM dark-field image of the annealed sample before deformation. The pillar is almost free of dislocations except a few remained near the top. (b) Initial deformation of the pillar by dislocation emission from the sources developed at the contact with the punch. (c) Emission of dislocations from another source developed at the bottom mount of the pillar. (d) A high density of dislocations emerges from the sources at both ends of the pillar. (e) TEM bright-field image after deformation to 33.2% strain. Multiple slip steps are evident, distributed homogeneously throughout the pillar with a spacing of ~ 30 nm, as some of them are indicated by black arrows. (f) SEM image of the deformed pillar showing the slip steps (black arrows). Note that the SEM image was recorded from another deformed pillar after the ex-situ microcompression test.

nucleation of dislocations was not localized to specific positions as in the FIB-prepared pillar, where single-armed sources were operating, but rather uniformly distributed over the whole pillar height (Fig. 9d). The nucleated dislocations slipped across the sample diameter and escaped through the opposite side surface without noticeable interaction, forming multiple surface steps over the whole specimen height (arrows in Fig. 9e and f), thereby accommodating up to 30% total plastic strain. The slip steps have an average step height of ~ 5 nm and were distributed over the whole length of the pillar with roughly ~ 30 nm spacing, in contrast to the strongly localized deformation of the FIB-prepared sample (Fig. 7 and Fig. 8).

Supplementary video related to this article can be found at <http://dx.doi.org/10.1016/j.actamat.2016.03.017>.

The different deformation behavior of the annealed Al pillars, i.e. a uniform deformation without pronounced slip localization, might be associated with the surface passivation by oxide formation. According to the atomic simulations by Sen et al., as an amorphous Al-oxide layer grows during annealing, the Al/Al-oxide interface

would develop an atomic-scale roughness on the surface of the Al nanowire, which increases the number of potential nucleation sites for dislocations [43,44]. In the context of dislocation nucleation, this Al/Al-oxide interface may promote rather uniform nucleation events along the pillar axis. However, it is currently difficult to identify potential nucleation sites for dislocations at the Al/Al-oxide interface by high-resolution TEM (refer to Fig. 10b) and correlate this with the measured stress values. Nonetheless, the above observations demonstrate that removing the FIB-induced dislocations by annealing facilitates multiple nucleation and unaffected escape of dislocations, resulting in a clearly different deformation characteristic as compared to that of the FIB-prepared pillars.

3.7. Role of the FIB-implanted Ga ions

It is worth to carefully analyze the distribution of implanted Ga in the Al pillars after annealing, as Ga could dissolve or precipitate a second phase. For this purpose, we carried out elemental mapping of an annealed pillar after deformation using STEM EDS. The results

reveal the presence of a high density of oxygen and Ga atoms near the surface (Fig. 10a). The line profile shown in Fig. 10b and c clarifies that the Ga atoms are confined below the oxide layer with the maximum concentration at ~ 7 nm from the surface, which agrees well with the ion trajectory simulation results in Fig. 1b. No second phase precipitation was noticed, which agrees well with the Al–Ga phase diagram indicating that the solubility of Ga in Al does not change much with temperature, i.e. 8.4 at.% at 500 K, and 8.3 at.% at RT. Thus, Ga should form a solid solution in the Al pillar.

We also note that there is a slightly higher Ga concentration at the top end of the pillar compared to the bottom base, as shown in the Ga elemental map in Fig. 10a. The EDS point spectra indicated that the Ga composition was ~ 4.7 at.% at the top end, while at the bottom part it was only ~ 1.9 at.%. One reason might be that the normal incidence of the Ga ion beam during the fabrication of pillar causes the implantation of more Ga on the top end of the pillar than the rest. However, we also note that the Gibbs-Thompson effect could possibly arise due to a curved top end (the effective radius is measured as ~ 10 nm in Fig. 10a), which increases the solubility of Ga compared to a flat top. Therefore, during annealing the implanted Ga atoms are likely to migrate towards the top end of the pillar, causing local enrichment therein. These enriched Ga atoms might act as obstacles for dislocation motions, resulting in residual dislocations even after annealing, as can be seen in Figs. 2e, 3a and 9a, and 11, which play a deterministic role in the initiation of plastic deformation. The local dislocation density measured along the pillar axis in the annealed pillars clearly shows that the dislocation density at the top part is in the order of $\sim 10^{13} \text{ m}^{-2}$. Interestingly, the

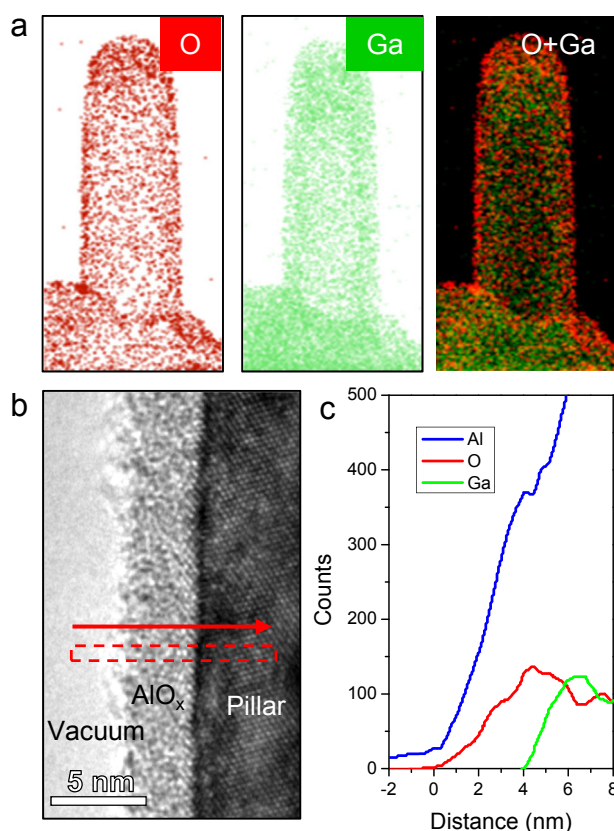


Fig. 10. (a) Elemental maps of an annealed Al pillar obtained by using STEM-EDS showing the spatial distribution of oxygen (left), Ga (middle), and their superposition (right). (b) HR-TEM image showing the formation of a surface oxide layer with a thickness of ~ 3 nm. (c) Line profile of the EDS maps along the direction indicated by the arrow.

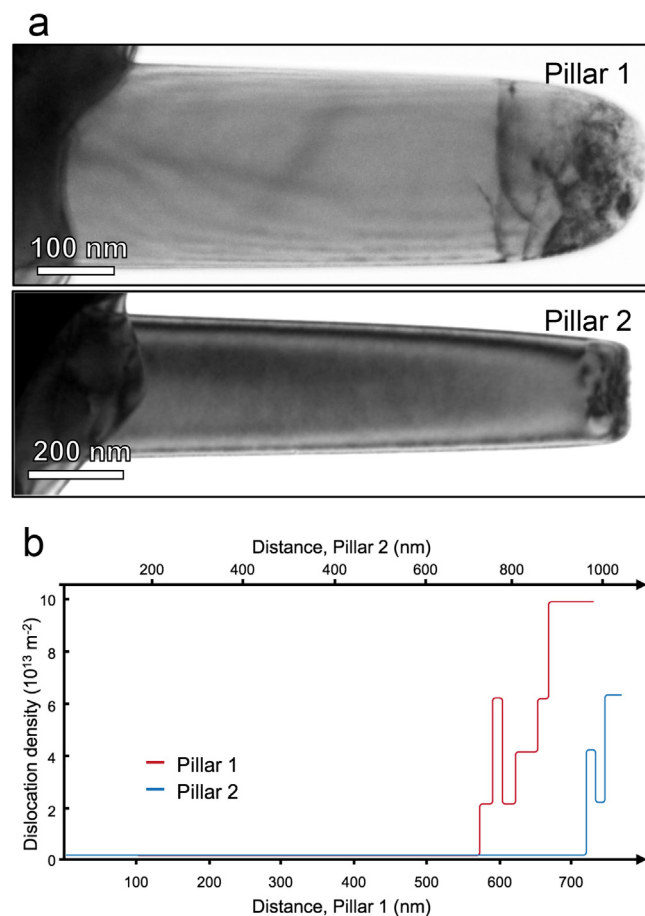


Fig. 11. (a) TEM images of annealed Al pillars showing the residual dislocations at the top end of the pillars. (b) Plot of the dislocation density for the two pillars shown in (a) along the axial direction. The dislocation density at the top part still remains in an order of $\sim 10^{13} \text{ m}^{-2}$.

dislocation density is higher in the pillar with a round top than that with a flat top end (refer to the different dislocation density in Fig. 11a and b). The high dislocation density at the top of the pillars, where the initial plasticity starts, supports that the small difference in yield stresses of both types of pillars is due to similar dislocation source structure. However, once dislocations are nucleated, they escape more easily in the annealed pillars than in the as-FIBed pillars resulting in clear differences in flow and strain burst behaviors as summarized in Fig. 4.

4. Conclusion

In the present study, vacuum annealing, as a method for removing FIB-induced defects in metal pillars, was carried out and its effect on the plastic deformation of single crystal Al pillars was investigated by performing microcompression tests and in-situ TEM compression experiments. We show that the Ga^+ ion beam induces structural damages near the surface, mostly in the form of interstitial type dislocation loops. Annealing of the FIB-prepared pillars at around half of the melting point effectively removes the dislocation loops by diffusion of thermally activated vacancies. In-situ TEM compression directly showed that the dislocation loops present in the FIB-prepared pillars play a critical role in governing not only the yield event, but also the flow behavior by blocking gliding dislocations and forming dislocation sources. The

subsequent plastic deformation becomes localized at the slip steps formed by continuous activation of these dislocation sources, forming dominant large slip steps. On the other hand, the annealed Al pillars exhibited rather uniform deformation characteristics by the formation of multiple fine slip steps due to the unhindered nucleation, propagation and exit of dislocations. Notably, the yield stress was not greatly altered by the annealing, since the residual dislocations present at the top end of the pillars predominantly determine the yield point. As exemplified by the present case of Al, annealing in high vacuum condition is effective in removing the FIB-induced defects, but still can result in surface oxidation, which may provide potential sites for dislocation nucleation by an additional surface roughening.

Acknowledgments

This work was supported by the National Research Foundation of Korea (NRF) grant funded by the Korea government (NRF-2015R1A2A2A01007904). Furthermore, DK acknowledges financial support by the Austrian Science Fund (FWF) via the projects I-1020 and P-25325.

References

- [1] M.D. Uchic, D.M. Dimiduk, J.N. Florando, W.D. Nix, Sample dimensions influence strength and crystal plasticity, *Science* 305 (2004) 986–989.
- [2] S.H. Oh, M. Legros, D. Kiener, G. Dehm, In situ observation of dislocation nucleation and escape in a submicrometre aluminium single crystal, *Nat. Mater.* 8 (2009) 95–100.
- [3] B. Wu, A. Heidelberg, J.J. Boland, Mechanical properties of ultrahigh-strength gold nanowires, *Nat. Mater.* 4 (2005) 525–529.
- [4] G. Richter, K. Hillerich, D.S. Gianola, R. Mönig, O. Kraft, C.A. Volkert, Ultrahigh strength single crystalline nanowhiskers grown by physical vapor deposition, *Nano Lett.* 9 (2009) 3048–3052.
- [5] J.R. Greer, C.R. Weinberger, W. Cai, Comparing the strength of f.c.c. and b.c.c. sub-micrometer pillars: compression experiments and dislocation dynamics simulations, *Mater. Sci. Eng. A* 493 (2008) 21–25.
- [6] J.Y. Kim, D. Jang, J.R. Greer, Tensile and compressive behavior of tungsten, molybdenum, tantalum and niobium at the nanoscale, *Acta Mater.* 58 (2010) 2355–2363.
- [7] S.M. Han, T. Bozorg-Grayeli, J.R. Groves, W.D. Nix, Size effects on strength and plasticity of vanadium nanopillars, *Scr. Mater.* 63 (2010) 1153–1156.
- [8] M.D. Uchic, P.A. Shade, D.M. Dimiduk, Plasticity of micrometer-scale single crystals in compression, *Annu. Rev. Mater. Res.* 39 (2009) 361–386.
- [9] J.R. Greer, J.T.M. De Hosson, Plasticity in small-sized metallic systems: intrinsic versus extrinsic size effect, *Prog. Mater. Sci.* 56 (2011) 654–724.
- [10] C.R. Weinberger, W. Cai, Surface-controlled dislocation multiplication in metal micropillars, *Proc. Natl. Acad. Sci. U. S. A.* 105 (2008) 14304–14307.
- [11] D. Kiener, A.M. Minor, Source truncation and exhaustion: Insights from quantitative in situ TEM tensile testing, *Nano Lett.* 11 (2011) 3816–3820.
- [12] J. El-Awady, Unravelling the physics of size-dependent dislocation-mediated plasticity, *Nat. Commun.* 6 (2015) 5926.
- [13] J.R. Greer, W.D. Nix, Nanoscale gold pillars strengthened through dislocation starvation, *Phys. Rev. B* 73 (2006) 245410.
- [14] B.D. Wirth, How does radiation damage, *Science* 318 (2007) 923–924.
- [15] J.P. McCaffrey, M.W. Phaneuf, L.D. Madsen, Surface damage formation during ion-beam thinning of samples for transmission electron microscopy, *Ultramicroscopy* 87 (2001) 97–104.
- [16] K. Thompson, D. Lawrence, D.J. Larson, J.D. Olson, T.F. Kelly, B. Gorman, In situ site-specific specimen preparation for atom probe tomography, *Ultramicroscopy* 107 (2007) 131–139.
- [17] J. El-Awady, C. Woodward, D. Dimiduk, N. Ghoniem, Effects of focused ion beam induced damage on the plasticity of micropillars, *Phys. Rev. B* 80 (2009) 104104.
- [18] H. Bei, S. Shim, M.K. Miller, G.M. Pharr, E.P. George, Effects of focused ion beam milling on the nanomechanical behavior of a molybdenum-alloy single crystal, *Appl. Phys. Lett.* 91 (2007) 111915.
- [19] S. Shim, H. Bei, M.K. Miller, G.M. Pharr, E.P. George, Effects of focused ion beam milling on the compressive behavior of directionally solidified micropillars and the nanoindentation response of an electropolished surface, *Acta Mater.* 57 (2009) 503–510.
- [20] D. Kiener, C. Motz, M. Rester, M. Jenko, G. Dehm, FIB damage of Cu and possible consequences for miniaturized mechanical tests, *Mater. Sci. Eng. A* 459 (2007) 262–272.
- [21] Z.W. Shan, R.K. Mishra, S.A. Syed Asif, O.L. Warren, A.M. Minor, Mechanical annealing and source-limited deformation in submicrometre-diameter Ni crystals, *Nat. Mater.* 7 (2008) 115–119.
- [22] M.B. Lowry, D. Kiener, M.M. Leblanc, C. Chisholm, J.N. Florando, J.W. Morris, et al., Achieving the ideal strength in annealed molybdenum nanopillars, *Acta Mater.* 58 (2010) 5160–5167.
- [23] D. Kiener, Z. Zhang, S. Šturm, S. Cazottes, P.J. Imrich, C. Kirchlechner, et al., Advanced nanomechanics in the TEM: effects of thermal annealing on FIB prepared Cu samples, *Philos. Mag.* 92 (2012) 3269–3289.
- [24] H. Zhang, B.E. Schuster, Q. Wei, K.T. Ramesh, The design of accurate micro-compression experiments, *Scr. Mater.* 54 (2006) 181–186.
- [25] D. Raabe, D. Ma, F. Roters, Effects of initial orientation, sample geometry and friction on anisotropy and crystallographic orientation changes in single crystal microcompression deformation: a crystal plasticity finite element study, *Acta Mater.* 55 (2007) 4567–4583.
- [26] L.A. Giannuyi, F.A. Stevie, *Introduction to Focused Ion Beams*, Springer Science & Business Media, 2005.
- [27] C.A. Volkert, A.M. Minor, Focused ion beam microscopy and micromachining, *MRS Bull.* 32 (2007) 389–399.
- [28] J.F. Ziegler, J. Biersack, U. Littmark, *The Stopping and Range of Ion in Matter*, 1985.
- [29] J.R. Greer, W.C. Oliver, W.D. Nix, Size dependence of mechanical properties of gold at the micron scale in the absence of strain gradients, *Acta Mater.* 53 (2005) 1821–1830.
- [30] Y. Kim, A.S. Budiman, J.K. Baldwin, N.A. Mara, A. Misra, S.M. Han, Micro-compression study of Al-Nb nanoscale multilayers, *J. Mater. Res.* 27 (2012) 592–598.
- [31] S.M. Han, M.A. Phillips, W.D. Nix, Study of strain softening behavior of Al-Al3Sc multilayers using microcompression testing, *Acta Mater.* 57 (2009) 4473–4490.
- [32] H. Idrissi, S. Turner, M. Mitsuhashi, B. Wang, S. Hata, M. Couliberty, et al., Point defect clusters and dislocations in FIB irradiated nanocrystalline aluminum films: an electron tomography and aberration-corrected high-resolution ADF-STEM study, *Microsc. Microanal.* 17 (2011) 983–990.
- [33] B.N. Singh, S.J. Zinkle, Defect accumulation in pure fcc metals in the transient regime: a review, *J. Nucl. Mater.* 206 (1993) 212–229.
- [34] M.J. Fluss, L.C. Smedskjaer, M.K. Chason, D.G. Legnini, R.W. Siegel, Measurements of the vacancy formation enthalpy in aluminum using positron annihilation spectroscopy, *Phys. Rev. B* 17 (1978) 3444–3455.
- [35] G. Ho, M.T. Ong, K.J. Caspersen, E.A. Carter, Energetics and kinetics of vacancy diffusion and aggregation in shocked aluminium via orbital-free density functional theory, *Phys. Chem. Chem. Phys.* 9 (2007) 4951–4966.
- [36] H.M. Polatoglou, M. Methfessel, M. Scheffler, Vacancy-formation energies at the (111) surface and in bulk Al, Cu, Ag, and Rh, *Phys. Rev. B* 48 (1993) 1877–1883.
- [37] D. Hull, D.J. Bacon, *Introduction to Dislocations*, Pergamon Press Oxford, 1984.
- [38] F. Mompou, M. Legros, A. Sedlmayr, D.S. Gianola, D. Caillard, O. Kraft, Source-based strengthening of sub-micrometer Al fibers, *Acta Mater.* 60 (2012) 977–983.
- [39] A. Kunz, S. Pathak, J.R. Greer, Size effects in Al nanopillars: single crystalline vs. bicrystalline, *Acta Mater.* 59 (2011) 4416–4424.
- [40] M. Kuroda, Higher-order gradient effects in micropillar compression, *Acta Mater.* 61 (2013) 2283–2297.
- [41] C. Motz, D. Weygand, J. Senger, P. Gumbsch, Initial dislocation structures in 3-D discrete dislocation dynamics and their influence on microscale plasticity, *Acta Mater.* 57 (2009) 1744–1754.
- [42] C.R. Weinberger, G.J. Tucker, Atomistic simulations of dislocation pinning points in pure face-centered-cubic nanopillars, *Model. Simul. Mater. Sci. Eng.* 20 (2012) 075001.
- [43] F.G. Sen, A.T. Alpas, A.C.T. van Duin, Y. Qi, Oxidation-assisted ductility of aluminium nanowires, *Nat. Commun.* 5 (2014) 3959.
- [44] S. Brochard, P. Hirel, L. Pizzagalli, J. Godet, Elastic limit for surface step dislocation nucleation in face-centered cubic metals: Temperature and step height dependence, *Acta Mater.* 58 (2010) 4182–4190.